095032

(14)

WATER RESOURCES RESEARCH, VOL. 39, NO. 8, 1225, doi:10.1029/2002WR001406, 2003

Are faults preferential flow paths through semiarid and arid vadose zones?

John M. Sigda and John L. Wilson

Department of Earth and Environmental Science, New Mexico Institute of Mining and Technology, Socorro, New Mexico, USA

Received 25 April 2002; revised 19 March 2003; accepted 19 May 2003; published 30 August 2003.

RECEIVED MAR 12 2007

[1] Numerous faults crosscut the poorly lithified, basin-fill sands found in New Mexico's Rio Grande rift and in other extensional regimes. The deformational processes that created these faults sharply reduced both fault porosity and fault saturated hydraulic conductivity by altering grains and pores, particularly in structures referred to as deformation bands. The resulting pore distribution changes, which create barriers to saturated flow, should enhance fault unsaturated flow relative to parent sand under the relatively dry conditions of the semiarid southwest. We report the first measurements of unsaturated hydraulic properties for undisturbed fault materials, using samples from a small-displacement normal fault and parent sands in the Bosque del Apache Wildlife Refuge, central New Mexico. Fault samples were taken from a narrow zone of deformation bands. The unsaturated flow apparatus (UFA) centrifuge system was used to measure both relative permeability and moisture retention curves. We compared these relations and fitted hydraulic conductivity-matric potential models to test whether the fault has significantly different unsaturated hydraulic properties than its parent sand. Saturated conductivity is 3 orders of magnitude less in the fault than the undeformed sand. As matric potential decreases from 0 to −200 cm, unsaturated conductivity decreases roughly 1 order of magnitude in the fault but 5–6 orders of magnitude in undeformed sands. Fault conductivity is greater by 2–6 orders of magnitude at matric potentials between −200 and −1000 cm, which are typical potentials for semiarid and arid vadose zones. Fault deformation bands have much higher air-entry matric potential values than parent sands and remain close to saturation well after the parent sands have begun to approach residual moisture content. Under steady state, one-dimensional, gravity-driven flow conditions, moisture transport and solute advection is 10^2–10^6 times larger in the fault material than parent sands. Faults are sufficiently conductive to hasten the downward movement of water and solutes through vadose-zone sands under semiarid and arid conditions like those in the Rio Grande rift, thereby potentially enhancing recharge, contaminant migration, and diagenesis. *INDEX TERMS:* 1875 Hydrology: Unsaturated zone; 8010 Structural Geology: Fractures and faults; 8045 Structural Geology: Role of fluids; 1829 Hydrology: Groundwater hydrology; 1832 Hydrology: Groundwater transport; *KEYWORDS:* fault, vadose zone, deformation band, hydraulic conductivity, unsaturated hydraulic properties, centrifuge

Citation: Sigda, J. M., and J. L. Wilson, Are faults preferential flow paths through semiarid and arid vadose zones?, *Water Resour. Res.*, *39*(8), 1225, doi:10.1029/2002WR001406, 2003.

1. Introduction

[2] Faults are common features in the poorly lithified clastic sediments of many extensional environments, such as the Rio Grande rift and the Basin and Range physiographic province. As in porous sandstones and crystalline rock, faults in poorly lithified clastic sediments can extend for tens of kilometers in length and meters in width. The physical expression of faults in such poorly lithified sediments can display core, damage, and mixed zones [*Heynekamp et al.*, 1999; *Rawling et al.*, 2001], which completely lack macroscopic fractures. This architecture differs substantially from the gouge-filled core zone and fracture-dominated damage zone architecture common to faults in crystalline rock [*Smith et al.*, 1989] and from the core zone and deformation band-rich damage zone described for faults in well-lithified porous sandstones [*Aydin*, 1978; *Antonellini and Aydin*, 1994; *Caine et al.*, 1996]. Deformation bands and zones of deformation bands are common elements within the damage and mixed zones of larger displacement faults in poorly lithified sediments [*Heynekamp et al.*, 1999; *Rawling et al.*, 2001] and may be the only visible element in smaller displacement faults [*Sigda et al.*, 1999; *Herrin*, 2001]. Deformation bands are narrow, quasi-tabular zones of localized deformation and diagenesis [*Aydin*, 1978; *Pittman*, 1981; *Edwards et al.*, 1993; *Sigda et al.*, 1999; *Cashman and Cashman*, 2000; *Herrin*, 2001]. Small displacement faults comprising only zones of deformation bands (called deformation band faults hereinafter) can be

Copyright 2003 by the American Geophysical Union.
0043-1397/03/2002WR001406$09.00

14672

locally numerous and extensive, both laterally and vertically. Deformation band faults in the variably lithified sands of the Rio Grande rift are poorly exposed and are not typically mapped at conventional geological scales (7.5 min quadrangle or larger).

[3] One commonly observed type of deformation band is formed by cataclasis (grinding and breaking of grains) and compaction, even from displacements as small as a few millimeters [*Aydin*, 1978; *Sigda et al.*, 1999; *Cashman and Cashman*, 2000; *Taylor and Pollard*, 2000; *Herrin*, 2001]. We do not consider noncataclastic deformation bands (i.e., compaction and dilation bands [*Antonellini et al.*, 1994]) because we have not observed them in the Rio Grande rift or found reports of their occurrence there in the literature. Cataclasis and compaction drastically reduce mean pore size, increase clay-size fraction, and decrease sorting, thereby reducing porosity and saturated hydraulic conductivity relative to parent sandstone [*Pittman*, 1981; *Antonellini and Aydin*, 1994; *Ogilvie et al.*, 2001] or parent sand [*Hong*, 1999; *Sigda et al.*, 1999]. The extent of reduction in porosity and saturated conductivity differs with degree of protolith (parent material) lithification. The porosity of deformation bands in sandstones is almost completely eliminated and saturated conductivity is reduced 1–7 orders of magnitude (relative to the protolith) [*Aydin*, 1978; *Fowles and Burley*, 1994; *Antonellini and Aydin*, 1994; *Ogilvie et al.*, 2001]. Deformation bands in poorly lithified sands demonstrate saturated conductivity decreases of only 2–4 orders of magnitude, and significant amounts of both macroporosity and microporosity remain [*Sigda et al.*, 1999; *Hong*, 1999; *Herrin*, 2001]. Irrespective of the degree of protolith lithification, deformation processes create sizeable structures with very different saturated hydraulic properties than the surrounding matrix.

[4] The striking changes in pore-size characteristics suggest that deformation band faults should differ significantly from their protolith in hydraulic properties beyond porosity and saturated hydraulic conductivity [*Sigda et al.*, 1999]. In particular, the dramatic reduction of pore size suggests that these faults retain relatively high water saturation even under dry conditions. Consequently, we raise two sets of questions: (1) Do deformation band faults have significantly different unsaturated hydraulic properties than their protolith? (2) Are these differences hydrologically significant under the relatively dry conditions of semi-arid and arid vadose zones? In particular, do these differences accelerate the movement of moisture, contaminants, or diagenetically important solutes through the vadose zone?

[5] Only the first of these questions has received any attention in the past, but solely for deformation band faults in well-lithified porous sandstone, and even then the focus was restricted to only one of the unsaturated hydraulic relationships of interest [*Antonellini and Aydin*, 1994; *Ogilvie et al.*, 2001] in the context of capillary barrier petroleum traps.

[6] To address these questions for poorly lithified sediments, we studied a small-displacement deformation band fault in the poorly lithified sand of central New Mexico's Rio Grande rift. Studying a small displacement fault allowed us to minimize the confounding effect of juxtaposition between different lithologies and so more clearly contrast the hydraulic behavior of the fault with that of its parent sand. We tested for differences in unsaturated hydraulic properties by measuring moisture content θ as a function of matric potential (or moisture potential, tension head, suction, and so forth) ψ, and unsaturated hydraulic conductivity K as a function of moisture content θ, for undisturbed samples of the deformation band fault and of the undeformed parent sand. Hydraulic property measurements were made with specially equipped centrifuges and then fitted to theoretical $\theta(\psi)$ and $K(\theta)$ models. We compared model fits and the resulting $K(\psi)$ relationships for both faulted and parent sand to investigate the potential for significant impacts on water and solute movement through the vadose zone. We have already noted that when potential $\psi = 0$, undeformed sand has roughly 2–4 orders of magnitude greater saturated hydraulic conductivity than the fault [*Sigda et al.*, 1999; *Hong*, 1999], but at some lower matric potential value (termed the crossover ψ value), the two materials have the same unsaturated conductivity because sand $K(\psi)$ decreases more rapidly than fault $K(\psi)$. As matric potential decreases further, the fault becomes more conductive than the sand. We use the fitted $K(\psi)$ relationships and a steady, gravity-driven flow model to show that faults should be preferred flow paths for both water and solutes under these dry conditions.

2. Geologic Setting

[7] Located near the southern end of the Rio Grande rift's Socorro basin in central New Mexico, our Canyon Trail field site includes two 135 m long outcrops separated by a railroad cut within the Bosque del Apache Wildlife Refuge, approximately 160 km south of Albuquerque, New Mexico (Figure 1a). The outcrops expose many faults crosscutting a poorly lithified, well-sorted, very fine to medium-grained buff sand overlain by a well-lithified, very poorly sorted, matrix-supported conglomerate containing large cobbles and boulders (Figure 1b). The conglomeratic unit is interpreted as a piedmont facies, while the sand unit comprises a lower bed of fine-grained sand, interpreted as an eolian facies, and an upper bed of medium-grained sand with a likely fluvial origin [*Hong*, 1999; *Herrin*, 2001]. Varying in thickness from 1 to 10 m where exposed, the sand is easily friable to the touch except for intermittent cementation, usually localized along bedding planes. Both conglomerate and sand units are interpreted as part of the Miocene-age Popotosa Formation (correlative with the Albuquerque Basin's lower Santa Fe Group), which forms the vadose and aquifer units in this area and in other parts of the Socorro and La Jencia basins [*Hawley*, 1978]. Poorly lithified, well-sorted, eolian and fluvial sands such as those found in our site area are common in Santa Fe Group basin fill throughout the Rio Grande rift region [*Hawley and Kernodle*, 2000]. Of particular importance are the major aquifer and vadose zone units in the Albuquerque, Las Cruces, and El Paso-Ciudad Juárez metropolitan areas [*Connell et al.*, 1999; *Hawley et al.*, 1995, 2001].

[8] Both east and west sand outcrops are cut by numerous deformation band faults and associated individual deformation bands (Figure 1b). Most clearly visible in the sand unit, individual deformation bands ($\leq$1 cm vertical displacement) closely resemble those described in other poorly lithified

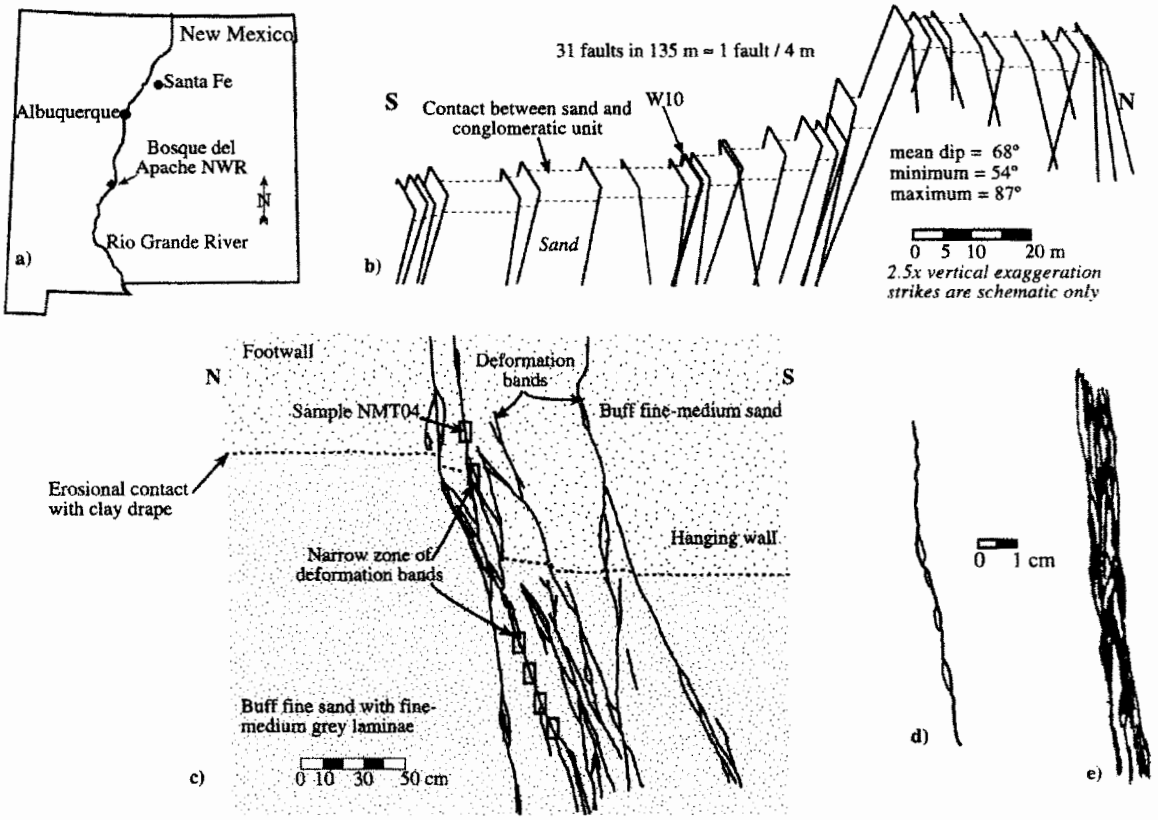

Figure 1. Site location and fault architecture. (a) Bosque del Apache National Wildlife Refuge, New Mexico. (b) Fault distribution and geology along west face of Canyon Trail field site. Each plane represents a mapped fault (true strikes not shown). (c) Site E10 (20 m east of fault W10 shown above in Figure 1b) showing assemblage of individual deformation bands and the narrow zone of deformation bands. Boxes show the locations of fault samples. Sand samples (not shown) were collected 3–3.5 m north of fault E10 (footwall) and 1.1–1.9 m south of fault (hanging wall). (d) Sketch of an individual deformation band. (e) Sketch of a narrow zone of deformation bands. Figures 1b, 1d, and 1e adapted from *Herrin* [2001].

Rio Grande rift sands [*Heynekamp et al.*, 1999; *Sigda et al.*, 1999]. Fault architecture varies from small displacement (≤1 m vertical displacement), mostly subparallel, narrow or diffuse zones of deformation bands in the south, such as those described by *Sigda et al.* [1999], to larger displacement faults (1 m < vertical displacement < 15 m) in the north with complex packages of deformation bands, zones of deformation bands, and pods of little-deformed sand that exhibit both subparallel and antithetical orientations [*Herrin*, 2001]. Roughly 30 faults have been identified in the sand unit, and although we did not count them all, we estimate there are hundreds to several thousand individual deformation bands located within and between fault zones. We attribute the observed average fault density of 1:4 m (one fault every 4 m) to the Socorro Basin having experienced as much as 50% extension during Oligocene and Miocene times [*Chamberlin and Osborn*, 1984; *Chapin and Cather*, 1994]. Fault dip varies between 54° and 87°, and displacement is predominantly normal with little evidence for strike slip [*Herrin*, 2001]. Fault width varies considerably along dip and along strike, as do the number and orientation of splays [*Herrin*, 2001]. Only one of the faults in the sand has been altered by cementation.

[9] We emphasize there are no open, macroscopic fractures within any fault in sand, although fractures are often found to cut through cobbles near faults in the conglomerate. Faults crosscutting both sand and conglomerate have a different appearance in the two units. Instead of the splaying, anastomosing distributions of deformation bands with highly variable widths and orientations observed in the sand, faults appear macroscopically as relatively linear tabular zones with reduced grain size and fairly consistent width and orientation in the conglomerate [*Herrin*, 2001].

[10] The eastern outcrop exposure of fault 10 (E10) was selected for intensive study because it possesses a small-displacement fault with a well-defined, vertically continuous, narrow zone of deformation bands within the sand unit (Figure 1c). Individual deformation bands were judged unsuitable for this study because they are too fragile and possess too little volume for effective measurements using the centrifuge method. Fault E10 crosscuts ~3 m of conglomerate and nearly 5 m of sand, which itself is divided

by an erosional contact (clay drape) into an upper bed of fine to medium grain buff sand roughly 3.5 m thick and a 1.5 m thick unit of fine grain buff sand with interbeds of slightly coarser gray sand (Figure 1c). The fault comprises a narrow zone of anastomosing deformation bands, which is a planar tabular structure varying between 0.5 and 1.5 cm in width and dipping 60 degrees, and an accompanying network of splaying deformation bands (Figures 1c–1e). These structural elements appear as white lineations, are better indurated than all but the cemented parent sand, and together have accommodated 55 cm of vertical displacement (Figure 1c).

3. Methods

3.1. Sample Collection

[11] Undisturbed samples of undeformed and faulted fine grain sand were collected from fault E10 and its footwall and hanging wall (Figure 1c) during two field seasons. The dimensions of the centrifuge rotors dictated sample sizes. Parent sand samples were cylindrical in shape with mean length and volume 5.3 cm and 68 cm^3 for large samples and 4.1 cm and 28 cm^3 for small samples. All five fault samples were hexahedral with mean length and volume 5.9 cm and 37 cm^3 for large samples and 4.9 cm and 16 cm^3 for small samples. Multiple sand samples were taken from the same (lower) bed on both E10's hanging wall and footwall. All but one of the fault samples were collected along the fault's down-dip length into which only materials from the same lower bed were entrained. The remaining fault sample, NMT04, was taken from the portion of the fault into which only the coarser upper sands were entrained (Figure 1c).

3.2. Sample Preparation

[12] Samples were carefully cut, then measured for bulk density using the clod method and oven-dry weight. Selected samples were jacketed with Devcon 2-Ton epoxy and then epoxied into Delrin sleeves to prevent short-circuiting of flow along the sample perimeter. One fault sample, DL02, was epoxied using the much denser Devcon F2 aluminum epoxy. Hexahedral fault samples were oriented so that flow through the sample was parallel to dip, reproducing down-fault flow. Flow was directed parallel to bedding (denoted hereinafter as $\text{bedding}_{\parallel}$) for nearly all sand samples because of difficulties in extracting intact samples with the longitudinal axis oriented normal to bedding (denoted as $\text{bedding}_{\perp}$). One pair of sand samples was successfully extracted from the footwall with longitudinal axes $\text{bedding}_{\parallel}$ (DS22) and $\text{bedding}_{\perp}$ (DS23). Different combinations (bottom assemblies) of plastic/stainless steel grids and filter paper/stainless steel filter mesh were joined to the sleeve bottoms to prevent sample slump or loss. Following transport to a lab in Richland, Washington, samples were saturated using a vacuum chamber with deaired Hanford vadose zone water [*Wright et al.*, 1994].

3.3. K-θ Relationships

[13] Centrifuge K-θ curves were measured using unsaturated flow apparatus (UFA) centrifuge systems (Beckman L8, J6, and J2 models) and the method described by Conca and others [*Conca and Wright*, 1990, 1992; *Khaleel et al.*, 1995; *Conca et al.*, 1999]. In this method, each of a pair of initially liquid-saturated samples is inserted into a sample bucket with an effluent collection chamber at the bottom, and then affixed to the UFA rotor. The samples are subjected to a stepwise-increasing series of angular velocities while applying a constant liquid flux to the inlet face of the sample via a proprietary liquid dispersion cap. Stored in the collection chamber after passing through the sample, effluent liquid is periodically weighed and emptied by stopping the centrifuge. Sample bucket design ensures that collection chamber effluent will not create any back-pressure as long as the centrifuge run time is carefully monitored. The liquid flux rate and angular velocity are held constant until the sample reaches steady state, and then the final average liquid content is gravimetrically determined. Steady state implies that the sample weight ceases to change and that volumetric moisture content is essentially uniform throughout the sample [*Nimmo et al.*, 1987]. The procedure is repeated after increasing the angular velocity ω to the next level and either maintaining or reducing the liquid flux rate (Table 1). In our experiments, the UFA was periodically stopped and samples were removed and weighed without sample buckets (to ensure greater accuracy) to determine whether sample weight had ceased changing. The distance from the axis of rotation to the outflow face was 10.73 cm for the large sample rotor and 11.73 cm for the small sample rotor. Sample weight was judged to be at steady state if the weight had changed by $\leq$0.05 gm, which represented 0.6–2.0% of saturation (saturation = 100%) for the smaller fault samples and 0.4–0.8% of saturation for the larger sand samples. Data recorded included centrifugation run times (to the nearest minute-average values for sand shown in Table 1), flux rate, sample weight, and weight of expelled water (all weights were measured to the laboratory scale's maximum accuracy of ±0.01 g).

Table 1. Unsaturated Flow Apparatus (UFA) Experimental Conditions

Rotor Speed, rpm	Microinfusion Pump Rate, mL/h	Average Run Time, hours
	K-θ Experimental Conditions	
300	50	4
600	50	4
1000	50	4
1500	50	4
2000	40	4
2000	15	8
2000	5	8
2000	1	8
2000	0.5	8
2300	0.2	12
2500	0.1	12
3000	0.01	12
	Rotor Speed, rpm	Minimum Run Time, hours
	ψ-θ Experimental Conditions	
	300, 600, 800	24
	1200, 1500, 2100, 3000, 4000, 5000, 7000, 9000	12

[14] Saturated hydraulic conductivity was measured at the start of each sample's K-θ experiment using the UFA centrifuge system as a constant head permeameter. A fully water saturated sample was spun at the minimum speed ($\geq$300 rpm, which is equivalent to a 50 cm head difference

for a small sample 5.3 cm long) required to establish steady flow. Volumetric flux rate was determined by measuring bubble travel times through the supply tubing. Weight measurements showed sample moisture content did not change appreciably, indicating that the measured hydraulic conductivity value was associated with a moisture content very close to saturation.

3.4. θ-ψ Relationships

[15] Centrifuge drainage curves were measured following *Hassler and Brunner*'s [1945] centrifuge method, adapted for the UFA. In this method, which has been a mainstay of petroleum core analysis laboratories since its introduction, an initially liquid-saturated sample is subjected to a stepwise-increasing series of angular velocities while carefully monitoring the change in liquid content. Air is allowed to freely enter the sample and leave the effluent collection chamber. Angular velocity is held constant until the capillary and centrifugal forces equilibrate, forcing liquid flux to zero, and then a final average liquid content is noted. The procedure is repeated after increasing the angular velocity to the next level (Table 1). In our experiments, sample weights were checked periodically by stopping the centrifuge to remove and weigh the samples without sample buckets. A sample weight was judged to have reached equilibrium conditions if the weight had changed by ≤ 0.05 g after at least several hours of centrifugation. We recorded centrifugation run times (to the nearest minute), sample weight, and weight of expelled water. The average moisture content-rpm data produced by an experiment were inverted to θ-ψ values using the method of *Forbes* [1994] as adapted for vadose zone hydrology conditions.

3.5. Fitting Models

[16] Theoretical models of unsaturated hydraulic properties were simultaneously fit to each sample's $K(\theta)$ and $\theta(\psi)$ data using a trial-and-error approach. Goodness of fit was subjectively determined by visual comparison of the fitted curves and data as parameter values were varied. We also applied the automatic curve fitting program RETC [*van Genuchten et al.*, 1991], but rejected its use as it typically yielded poor fits. The commonly used Mualem-van Genuchten (MvG) theoretical model was fit to the UFA data for each sample [*Mualem*, 1976; *van Genuchten*, 1980]:

$$\theta(\psi) = \theta_r + (\theta_s - \theta_r)(1 + |\alpha\psi|^n)^{-m} \tag{1}$$

where $m = (n - 1)/n$

$$K(\theta) = K_s\left(\frac{\theta - \theta_r}{\theta_s - \theta_r}\right)^{\beta} \cdot \left(1 - \left(1 - \left(\frac{\theta - \theta_r}{\theta_s - \theta_r}\right)^{1/m}\right)^{m}\right)^2 \tag{2}$$

where K_s is the saturated hydraulic conductivity ($L\,T^{-1}$), α is the inverse of the air entry matric potential (L^{-1}), θ_s is saturated volumetric moisture content ($L^3\,L^{-3}$) and equals the connected porosity for vacuum saturation, θ_r is the residual volumetric moisture content ($L^3\,L^{-3}$), and n and β are dimensionless fitting parameters. The n parameter is an index of the pore size variability (commonly taken as the inverse of the pore size standard deviation) for the MvG model, whereas β represents the tortuosity and the partial correlation in pore radius between two adjacent pores at a given saturation [*Mualem*, 1976]. During parameter fitting we constrained the measured parameters, K_s, α, θ_s, and θ_r, much more than the n and β fitting parameters. Once the data were fitted to these two equations, the $K(\psi)$ relationship was easily calculated. The *Brooks and Corey* [1964] model was also fit to the experimental data, but, having yielded very similar results, is not reported here [see *Sigda*, 2003].

[17] We calculated a set of parameter values that correspond to a "mean" undeformed sand and to a "mean" fault by averaging estimated values for each parameter across all samples for each material. Thus the mean fault α is the arithmetic average of the set of α values estimated for all fault samples. Mean values for the θ_s, θ_r, n, and β parameters were calculated in the same fashion. Mean saturated hydraulic conductivity K_s was calculated by geometric averaging of the estimated K_s values.

3.6. Potential Hydrologic Relevance

[18] Our preliminary assessment of the potential hydrologic significance of deformation band faults used a simple, one-dimensional, analytical model of steady flow. We chose an analytical modeling approach because it grasps the essential features of the second research question without introducing conceptual complexity. We calculated and compared downward moisture and solute movement in the fault and in the parent sand. A numerical model should be used to examine other factors influencing the hydrologic importance of faults, such as transient flow, fault architecture, spatial density, dip, and other spatially varying characteristics, but it will introduce approximation issues. In particular, numerical approximations must resolve the effects of large hydraulic property changes over the subcentimeter scale while modeling flow in domains that extend for tens of meters (see Figure 1).

[19] The unsaturated hydraulic conductivity is numerically equal to the liquid-phase flux density (specific discharge) when faults are vertical, there is no exchange of moisture between fault and sand, and the hydraulic behavior is sufficiently constant over long time periods to be considered steady state. Such conditions are most likely to be found in the middle portion of a thick, arid or semiarid vadose zone, well below the root zone and well above the capillary fringe, where gravity, as the sole driving force, induces a unit gradient. Steady downward liquid-phase advection of water and solute is thus determined by the ambient matric potential, which is assumed to be constant, and the material's $K(\psi)$ relation. Under these assumptions, the liquid-phase flux density, q_l, is given by

$$q_l(\psi) = K(\psi) = K_s(1 + |\alpha\psi|^n)^{-m\beta} \cdot \left\{1 - \left[1 - (1 + |\alpha\psi|^n)^{-1}\right]^{-m}\right\}^2 \tag{3}$$

Advective transport of nonreactive, nonvolatile solutes is calculated using the seepage velocity, defined as the flux density (3) divided by the effective moisture content: q_l/θ_{eff}. As a simplification, we approximate the effective moisture content by the total volumetric moisture content for the governing matric potential: $\theta_{eff} = \theta(\psi)$. Rather than examine velocity we studied solute advective residence time

Table 2. Measured Properties

Sample ID	Description[a]	Sample Volume, cm^3	Bulk Density, g/cm^3	Porosity, cm^3/cm^3	Saturated Hydraulic Conductivity, cm/s
		Footwall			
DL06	buff	73.8	1.68	0.31	1.2×10^{-3}
DS08	gray	34.9	1.67	0.30	2.2×10^{-3}
DS22	buff and gray ‖ to bedding	24.7	1.70	0.30	2.3×10^{-3}
DS23	buff and gray ⊥ to bedding	25.6	1.66	0.29	2.1×10^{-3}
	all lower bed samples		1.68 ± 0.02 (5)[b]	0.30 ± 0.01 (4)	$1.9 \times 10^{-3} \pm 0.13$ (4)
	all upper bed samples		1.81 ± 0.02 (2)	0.30 ± 0.01 (2)	NM[c]
		Hanging Wall			
DL07	buff and gray	62.0	1.63	0.33	1.1×10^{-3}
DS07	buff and gray	29.2	1.61	0.31	2.0×10^{-3}
NMT15	buff	23.7	1.63	0.31	NM
	all lower bed samples		1.66 ± 0.05 (7)	0.32 ± 0.02 (3)	$1.5 \times 10^{-3} \pm 0.18$ (2)
	all upper bed samples		1.75 ± 0.03 (3)	0.31 ± 0.02 (2)	NM
		Fault			
DL02	lower fault	38.1	1.94	0.21	9.5×10^{-6}
DL20	lower fault	36.2	1.91	0.20	3.5×10^{-6}
NMT11	lower fault	12.9	1.89	0.20	3.7×10^{-6}
NMT18	lower fault	20.0	2.04	0.20	8.3×10^{-6}
	all lower bed ZDB[d] samples		1.95 ± 0.07 (4)	0.20 ± 0.01 (4)	$5.7 \times 10^{-6} \pm 0.23$ (4)
NMT04	above erosional contact	15.0	1.95	0.22	2.0×10^{-5}
	all upper bed ZDB samples		1.95 ± 0.01 (2)	0.24 ± NA[c] (1)	$1.96 \times 10^{-5} \pm$ NA (1)

[a]Buff sand is very fine to fine grained; gray sand is fine to medium grained.
[b]Mean ± standard deviation and (number of samples). K_s statistics are calculated for the base 10 logarithms of the measured values. The (geometric) mean K_s value shown is the back-transformed mean log value, but the standard deviation shown is the standard deviation of the logarithms. (The sixth fault sample has only a bulk density measurement due to time constraints.) Aggregate statistics for sand beds and faults are based on all samples for which any measurements were made, not just those samples for which UFA analyses were completed.
[c]NM, not measured; NA, not applicable.
[d]Zone of deformation bands.

t_r (years). For a vertical column of length L (cm) this is given by

$$t_r(\psi) = L/v_s(\psi) = L\theta(\psi)/q_l(\psi) \tag{4}$$

where v_s is the seepage velocity (cm/yr) and θ is the volumetric moisture content (cm^3 cm^{-3}). The advective residence time depends on the domain's ambient matric potential.

4. Results

[20] Nearly two dozen samples were collected from the fault E10 site during two field seasons. Six samples were collected from the fault, seven from the footwall sand, and 10 from the hanging wall sand. Measurements for all properties were successfully completed on slightly over half of these samples (Table 2).

[21] Undeformed sand samples appear quite similar in bulk density, porosity, and saturated hydraulic conductivity K_s, for both hanging and foot walls, with a slight difference in bulk density between the upper and lower sand beds (Table 2). The UFA K_s results for hanging wall and footwall sands are quite close to *Hong*'s [1999] water permeameter measurements and our unpublished air minipermeameter measurements made on the same units near fault E10.

[22] The fault samples also have very similar porosity and bulk density values, but the sample from the coarser-grained upper sand bed, NMT04, has a larger K_s than that observed in the lower bed samples (Table 2). Fault samples have greater bulk density and lower porosity than their parent sands. Comparison of K_s measurements between fault and parent sand demonstrates that parent sand K_s is 2 to approximately 3 orders of magnitude larger than fault K_s. This pattern corroborates previous observations made at Canyon Trail's fault E10 site [*Hong*, 1999] as well as other deformation band fault sites in the Rio Grande rift, such as the Santa Ana site in the Albuquerque Basin of New Mexico [*Sigda et al.*, 1999]. Our UFA centrifuge K_s measurements also compare very well with *Hong*'s [1999] flexible-wall water permeameter measurements for materials from the fault E10 site.

[23] Eleven intact samples were used in both K-θ and θ-ψ experiments (Table 2). Only θ-ψ data were measured for hanging wall sample NMT15. The θ-ψ experiments for two samples, DS22 and DS23, were not executed according to protocol and may not have fully achieved equilibrium conditions. The θ-ψ data for DS22 were discarded because the sample dried out prematurely, making it impossible to fit model parameters. We retained DS22's K-θ data for comparison. K-θ experiments for 11 samples yielded ranges of $0.07 \leq \theta \leq 0.33$ and $10^{-9} \leq K \leq 10^{-3}$ cm/s for undeformed sand, and $0.13 \leq \theta \leq 0.24$ and $10^{-9} < K < 10^{-5}$ cm/s for faults (Figure 2). The UFA method has been reported able to measure hydraulic conductivity as low as $\sim 10^{-10}$ cm/s [*Conca and Wright*, 1998], but all our measurements less than 10^{-9} cm/s were rejected because of a procedural error. The θ-ψ experiments for 11 samples yielded ranges of $0.06 \leq \theta \leq 0.24$ for faults, $0.04 \leq \theta \leq 0.34$ for undeformed sand, and $-5.0 \times 10^5 < \psi < 0$ cm for all samples (Figure 2). Replicate θ-ψ experiments for fault sample DL02 show good agreement (see Figure A1).

[24] Each of the samples with complete analyses was parameterized for the Mualem-van Genuchten (MvG)

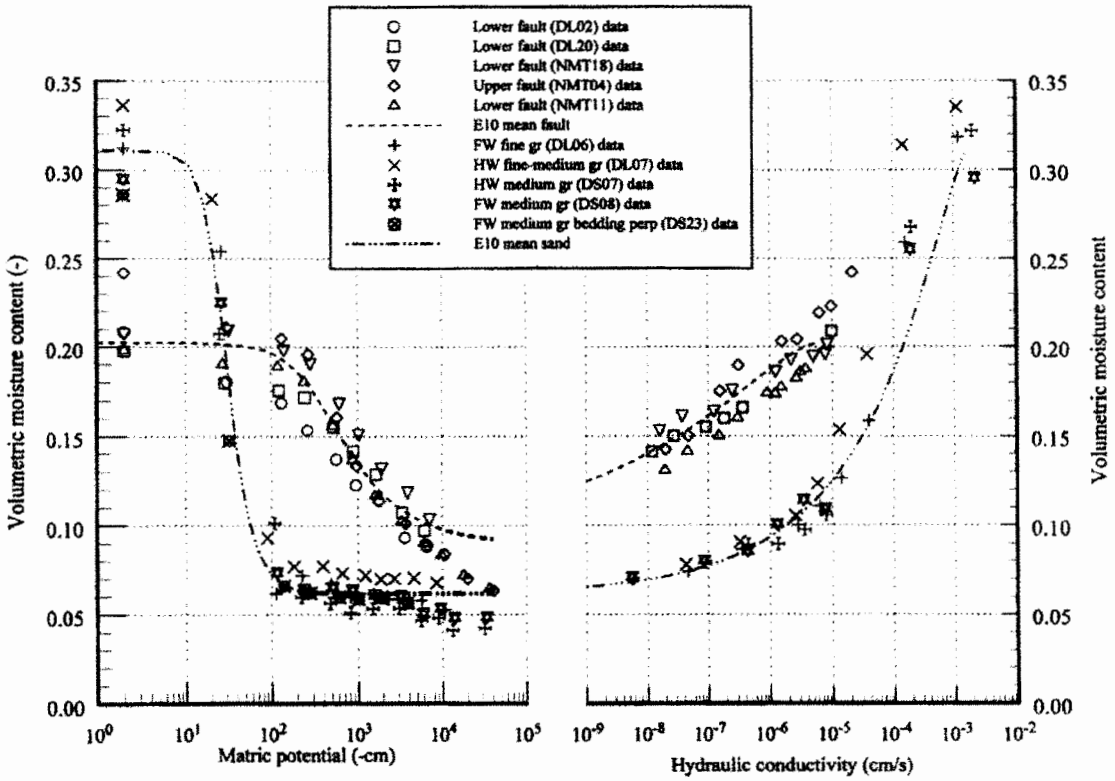

Figure 2. UFA measurements of unsaturated hydraulic relations. The θ-ψ results are shown on the left; K-θ results are shown on right. Dashed lines show the fitted curves for the fault E10 mean sand and mean fault set of parameters.

models for K-θ and θ-ψ by simultaneously fitting equations (1) and (2). The results are reported in Table 3; plots of individual fits are shown in Appendix A. Fitted and measured K_s values were not constrained to match exactly, and estimates of the θ_s and θ_r parameters were selected to give the best overall fit to both K-θ and θ-ψ curves. If fitted independently, estimates of residual moisture content (θ_r) were typically higher for the K-θ than the θ-ψ curves, particularly for the last several centrifuge speed steps (Appendix A). Variability in water storage volume and drainage behavior of the sample holder's bottom assembly, particularly those that used filter papers, had a significant influence on saturated moisture content (θ_s) for smaller samples. We used data from control experiments on empty sample holders to minimize the confounding influence of bottom assembly drainage from sample data, but disparities as small as 0.01 units of volumetric moisture content in θ_s significantly enlarge the feasibility space for n and β parameter estimates [*Sigda*, 2003]. It was not possible to fit the MvG (or Brooks and Corey) model to closely match the K-θ data just below saturation and still maintain a reasonably good fit at middle and lower saturation for the sand samples; however, this was seldom a problem for fault samples (Appendix A).

[25] Fault air entry matric potential values (α^{-1}) range between −250 and −450 cm of matric potential and are 10–20 times greater than the −20 to −30 cm values estimated

Table 3. Fitted Parameter Values for Mualem-van Genuchten Model

Sample ID	θ_s	θ_r	α, 1/cm	n	β	K_s,[a] cm/s
			Footwall Sand			
DL06	0.315	0.058	0.03	3.4	0.2	1.20×10^{-3}
DS08	0.300	0.062	0.035	3.2	0.7	2.40×10^{-3}
DS23	0.287	0.060	0.046	2.9	0.8	2.20×10^{-3}
			Hanging Wall Sand			
DL07	0.335	0.07	0.034	3.5	0.1	1.20×10^{-3}
DS07	0.320	0.058	0.045	3.7	0.3	2.00×10^{-3}
Mean	0.318	0.062	0.038	3.34	0.42	1.72×10^{-3}
SD	0.014	0.005	0.01	0.30	0.31	1.46×10^{-1}
			Fault			
DL02	0.196	0.105	3.2E-03	1.80	0.9	9.9×10^{-6}
DL20	0.198	0.105	4.0E-03	1.80	1.2	3.5×10^{-6}
NMT11	0.190	0.075	2.2E-03	1.80	1.1	3.8×10^{-6}
NMT18	0.200	0.085	2.8E-03	1.55	2.7	8.3×10^{-6}
NMT04	0.227	0.075	3.5E-03	1.75	1.9	2.0×10^{-5}
Mean	0.202	0.089	0.003	1.74	1.56	7.36×10^{-6}
SD	0.014	0.015	0.001	0.11	0.74	3.15×10^{-1}

[a]Mean and standard deviation for K_s are calculated for the base 10 logarithms of the estimated values. The (geometric) mean value shown is the back-transformed mean log value, but the standard deviation shown is the standard deviation of the logarithms.

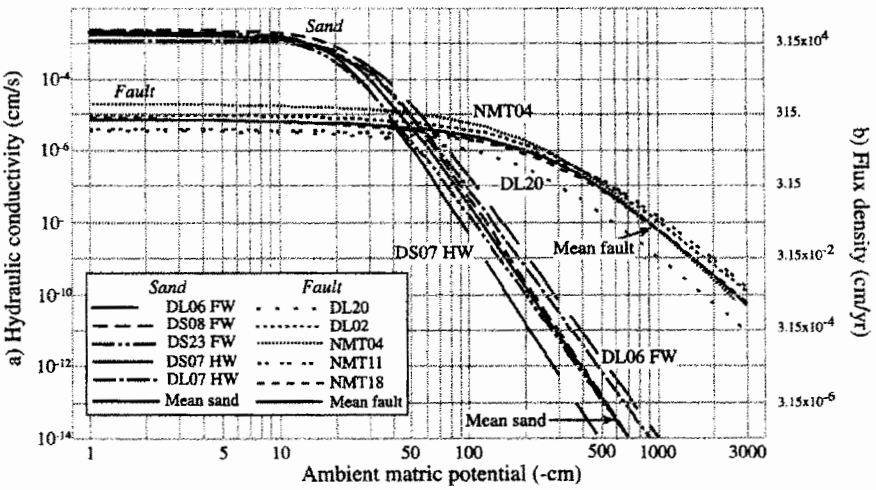

Figure 3. (a) K-ψ relationships for fault E10 from fitted Mualem-van Genuchten parameters. FW denotes footwall; HW denotes hanging wall. (b) The liquid-phase downward flux density for gravity-driven flow, $q_l(\psi) = K(\psi)$.

for undeformed sand samples (Figure 2 and Table 3). Estimates of the MvG scaling variables n and β show consistent differences between fault and sands. Sands have n values close to three, whereas fault values fall between one and two (Table 3). In contrast, sand β values are always less than fault β values and are reasonably close to the 0.5 estimated by *Mualem* [1976] for 45 different soils (Table 3). Fault β values appear more variable than those for sands and are consistently larger than the commonly assumed value of 0.5.

[26] K-ψ curves calculated from fitted MvG parameters show significantly different unsaturated behaviors for parent sand and deformation band faults (Figure 3). Sand K rapidly decreases 2 orders of magnitude once matric potentials drop below the sand air entry potential, reaching a crossover ψ (between -35 and -80 cm) where sand conductivity equals the fault conductivity (Figure 3). Below this crossover ψ, the sand conductivity K is much more sensitive to matric potential than the fault, so that sand K is at least 4 orders of magnitude less than fault K at $\psi = -500$ cm. K-ψ plots for the mean fault and the mean sand fall near the middle of the appropriate set of material curves and so adequately describe "average" sand and fault behaviors (Figure 3). Fault sample NMT04, which had the largest parent sand grain size, maintains an appreciably larger hydraulic conductivity across much of the ψ range. We observed little systematic difference between large volume (DL) and small volume (DS and NMT) samples.

[27] Sand saturated conductivity K_s is lower for the bedding$_\perp$ DS23 sample than the bedding$_\parallel$ DS22 sample, and though the margin of difference is somewhat smaller than that determined by *Hong* [1999], it is still larger than the observed variability in experimental flow rates (coefficients of variation = 3% for both DS22 and DS23). Our sand K_s anisotropy estimate of 0.92 is smaller than Hong's estimate of 0.66, which was based on more numerous measurements. We found that for moisture contents less than saturation, bedding$_\perp K(\theta)$ (DS23) is larger than bedding$_\parallel K(\theta)$ (DS22) (Appendix A). This difference may be real, if unexpected, but the close agreement in ψ-θ and K-θ data between the bedding$_\perp$ DS23 sample and two other bedding$_\parallel$ footwall samples, DL06 and DS08, suggests that the DS22 data may have been compromised by unknown error. While we have no measurements of anisotropy in the fault, *Hong* [1999] measured K_s anisotropy in a narrow zone of deformation bands. He found that saturated anisotropy is much larger than that for the parent sands; normal-to-dip fault K_s is only 10% of parallel-to-dip fault K_s.

[28] The K-ψ plot (Figure 3) also describes how the sand and fault gravity-driven, liquid-phase flux densities vary with matric potential. Below the ψ crossover of -35 to -80 cm, fault liquid-phase flux density exceeds sand liquid-phase flux density by orders of magnitude so that gravity-driven steady infiltration through the fault far exceeds infiltration through the adjacent sand. Thus gravity-driven, steady infiltration is 10–1000 times faster through the deformation band fault than the parent sand whenever $\psi = -100$ cm, and at -500 cm, the flux density disparity increases to between 10^4 and 10^6. Advective solute residence times t_r increase much more rapidly for sand, as matric potential decreases, than for faults (Figure 4). At high matric potentials, sand residence time is 2 orders of magnitude shorter, but sand and fault residence times t_r are equivalent for slightly dryer conditions, $-40 \leq \psi \leq -90$ cm. At $\psi = -200$ cm fault t_r increases by less than an order of magnitude from its value at $\psi = 0$, yet sand t_r increases by 5–7 orders of magnitude over the same interval.

5. Discussion

[29] The measured values of porosity and saturated hydraulic conductivity confirm previous findings that deformation band faults have much lower porosity and saturated conductivity K_s values than their parent sands. In our fault E10 samples, saturated hydraulic conductivity is shown to be $\sim 10^{-3}$ cm/s for flow through poorly lithified sands oriented bedding$_\parallel$ and $\sim 10^{-6}$ to $\sim 10^{-5}$ cm/s for narrow zones of deformation bands with flow oriented parallel to

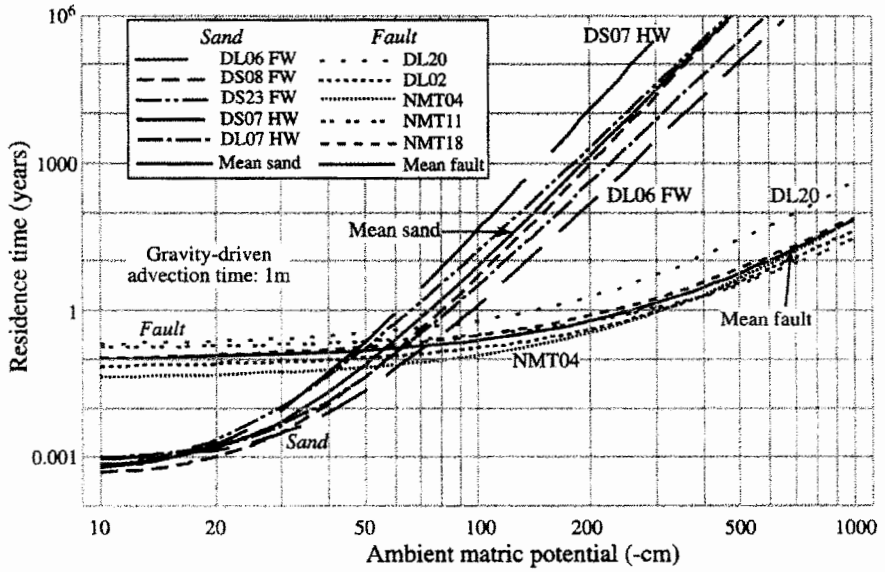

Figure 4. Solute residence time as a function of the matric potential for fault E10 samples. Gravity-driven residence time, t_r (years), for a conservative solute to travel 1 m with no dispersion.

dip (Table 2). In comparison, *Hong* [1999] measured K_s values for bedding$_{\|}$ flow of $2.3-9.1 \times 10^{-3}$ cm/s in fault E10 footwall and hanging wall finer-grained sands, and values of $2.5-3.7 \times 10^{-7}$ cm/s for flow oriented normal to fault E10 deformation bands.

[30] In answer to our first research question, the centrifuge data and model fitting support the hypothesis that deformation band faults have significantly different unsaturated hydraulic properties than their parent sands. Deformation band faults possess smaller pores and greater variability in pore sizes, leading to higher residual moisture contents and higher air entry matric potential values than their poorly lithified parent sands. The van Genuchten n parameter, which is proportional to the inverse of the pore size distribution's standard deviation, is much lower for fault than sand. This difference in fitted n values is supported by previous thin section observations that grain and pore sizes are much more variable in deformed than undeformed sediments [*Sigda et al.*, 1999; *Herrin*, 2001]. The large difference in air entry values indicates that faults remain near saturation or have higher moisture contents when adjacent sands have almost entirely drained. Higher θ_r values for faults suggest that faults contain a vertically and horizontally continuous network of wholly or nearly saturated pores within the individual deformation bands even under dry vadose zone conditions of -100s of centimeters of matric potential.

[31] Sand unsaturated hydraulic conductivity drops 6 orders of magnitude as matric potential decreases from 0 to -200 cm, whereas fault conductivity decreases only 1 order of magnitude over the same ψ range and remains close to saturation. At a matric potential of -500 cm, fault conductivity exceeds sand conductivity by at least 4 orders of magnitude. Whereas sand samples begin draining at $\psi = -30$ cm and reach residual moisture content near $\psi = -200$ cm, fault samples do not drain appreciably until ψ reaches -200 cm, and do not approach residual moisture content until ψ is less than $-10{,}000$ cm (Appendix A). The ψ-θ, K-θ, and K-ψ relationships are consistent for all sand samples, indicating no appreciable differences between hanging wall and footwall samples (Figure 2 and Appendix A). Even though NMT04 is not directly comparable to the other four fault samples because it was formed from the coarser upper sand and has a K_s at least twice that of the next most conductive sample, the five fault samples display consistent K-ψ relations. Choice of theoretical model, Mualem-van Genuchten or Brooks and Corey, has no impact on the relative differences in sand and fault behavior [*Sigda*, 2003].

[32] Our observations may hold for similar types of deformation structures in poorly lithified sand. Although our measurements were restricted to centimeter-wide zones containing numerous deformation bands, it is reasonable to speculate that individual deformation bands ($\sim$1–2 mm in width), which are often very numerous, may demonstrate similar hydraulic behavior because they are also created by compaction and cataclasis. We also speculate that deformation band faults in medium and coarse sands will show larger relative differences in unsaturated properties than those we have reported here for fine sands. This assumes that deformed grain size is independent of parent grain size for the bulk of the protolith. The larger mean pore sizes for coarse or medium grain undeformed sand are likely to have much larger van Genuchten n values and lower air entry potentials which would cause the K-ψ crossover to occur at larger matric potentials (nearer to zero) and lead to greater differences between fault and parent sand.

[33] While this paper is the first work investigating the unsaturated flow properties of faults in poorly lithified sands, there is previously published work on the petroleum reservoir capillary sealing properties of cataclastic deformation band faults in well-lithified porous sandstones. *Antonellini and Aydin* [1994] used image analysis to

estimate pore sizes for interconnected pores in both deformation bands and protolith. They estimated air entry matric potential for these faults as 1–2 orders of magnitude larger than that for the protolith. *Ogilvie et al.* [2001] used mercury porosimetry to measure the drainage capillary pressure-saturation relationships (analogous to the ψ-θ relationship) of protolith and a narrow zone of deformation bands. Their results yielded a 9% fault porosity, 20% sandstone porosity, and a fault air entry matric potential of the order of 40 m versus a value no larger than 4 m for the sandstone protolith, again about an order of magnitude difference. The air entry values in these studies are much larger than those estimated for the poorly lithified sand (~30 cm) and faults (~300 cm) in this study because of the great differences in lithology, diagenesis, and pore networks. Yet the relative differences in air entry value between protolith and fault are similar, that is, about an order of magnitude or more. The *Ogilvie et al.* [2001] capillary pressure-saturation curves (their Figure 2b) for a well-lithified sandstone and fault are quite similar in shape to the ψ-θ curves (Figure 2; Appendix A) that we report in this paper for poorly lithified sand and fault. Neither sandstone study investigated the relationship between hydraulic conductivity and moisture content (relative permeability curve), and their results cannot be used to address our second research question (see below), i.e., Do these faults significantly affect variably saturated fluid flow?, without making additional assumptions about the K-θ relationship.

[34] Measuring both ψ-θ and K-θ relationships with the UFA centrifuge is relatively new [e.g., *Flint et al.*, 1999; this study], so we note several procedural issues that we encountered in the hopes of improving the methodology. Porosity and drainage characteristics of the sample holder's bottom assembly must be determined and, if possible, the volume stored at any time be minimized, especially for small sample volumes. Proper choice of bottom assembly materials will help ensure that θ_s estimates from separate ψ-θ and K-θ experiments will match closely, thus simplifying estimation of the K-ψ model's scaling parameters, e.g., the n and β parameters in the Mualem-van Genuchten model. The moisture retention data and fits demonstrate that the centrifuge schedule of angular velocities (Table 1) captured most of the drainage behavior for the fault samples, but missed much of the sand's midsaturation behavior (Figure 2 and Appendix A). Increasing the number of experimental steps at low centrifuge speeds should improve resolution of the moisture retention curves for sands and reduce data loss during data inversion using the method of *Forbes* [1994] (or other similar methods). Our data also suggest that high centrifuge speeds (>5000 rpm) may induce moisture loss through evaporation, losing the expected balance between matric forces and the centrifugal body force. Another problem is our inability to fit the MvG model to the sand 300 and 600 rpm experimental steps for K-θ. This was not a problem for most fault samples, which required centrifuge speeds $\geq$1000 rpm to induce flow. Perhaps a hydraulic steady state had not been achieved in the sand even though sample weight changed by $\leq$0.05 g, or the Mualem-van Genuchten model does not fit these materials very well near saturation. It is also likely that the experiment's principal assumption that the centrifugal body force gradient is far greater than the matric potential gradient [*Nimmo et al.*, 1987; *Conca and Wright*, 1990, 1992] has been violated.

[35] Although we can only begin to answer our second question, the observed differences in hydraulic properties already suggest that faults have a significant hydrologic impact under relatively dry climatic conditions. Under those conditions and using the hydraulic properties described here, the simple, gravity-driven, steady flow model predicts downward, liquid-phase flux densities that are 10^2–10^5 times larger in faults than in their parent sands (Figure 3), and reduce nonreactive solute travel times by similar orders of magnitude (Figure 4). Such an enormous disparity between sand and fault behavior increases the likelihood that deformation band faults act as preferential flow paths through vadose zones with steady matric potentials in the range of −100 to −2000 cm. Determining the extent of faults' hydrologic importance requires further investigation to consider, among other things, ambient matric potential conditions, moisture and solute exchange between fault and sand, the role of competing processes, as well as fault architecture, dip, and spatial density.

[36] Ambient matric potential data for the Rio Grande rift indicate that preferential liquid-phase flow through faults can occur, but is likely to be spatially variable. Most measurements of shallow ambient matric potentials for this area are in the tensiometer range: $0 \leq \psi \gtrsim -600$ cm [*Stephens and Knowlton*, 1986; *Mattson*, 1989; *McCord et al.*, 1991; *Brainard et al.*, 2002], a wetter subset of the range considered in this paper. In combination with the $\psi(\theta)$ relations estimated in this study, our own measurements of in situ moisture content demonstrate that the near-surface matric potential is between −180 and −380 cm (Appendix B). In contrast, data from a recent Albuquerque Basin infiltration experiment revealed drier conditions with matric potential values well below the tensiometer range in the top 8 m [*Brainard*, 1997], likely indicating liquid-phase infiltration through sand is negligible at that location. Vapor-phase flux eventually becomes more important than liquid-phase flux as sand becomes sufficiently dry. Thermal vapor-phase flux density values have been estimated to fall between 1.0 and 3.0×10^{-3} cm/yr (compare to right-hand axis of Figure 3) for other arid vadose zones in the American Southwest [*Ross*, 1984; *Scanlon et al.*, 1997]. For a certain range of drier conditions, it is likely that water transport through the sand is dominated by vapor-phase processes, whereas the faults could still be dominated by liquid-phase transport. The dominant mechanism for solute movement through the sand should also switch, from advection to diffusion, as matric potential drops. Solute transport through the fault could still be dominated by the advection considered here, until much lower matric potentials are reached.

[37] Although deformation band faults appear to provide a liquid-phase "fast path" for water and solutes through the sandy parts of the Rio Grande rift vadose zone, it is still not clear whether such "fast paths" are significant. The minimum fault density required to affect groundwater recharge may only occur in a small portion of the Rio Grande rift. There are clearly areas with no faults, but we and others [e.g., *Carter and Winter*, 1995; *Grauch*, 2001] have found many locations in the Rio Grande rift with moderate to high densities of faults, such as the Canyon Trail site of this

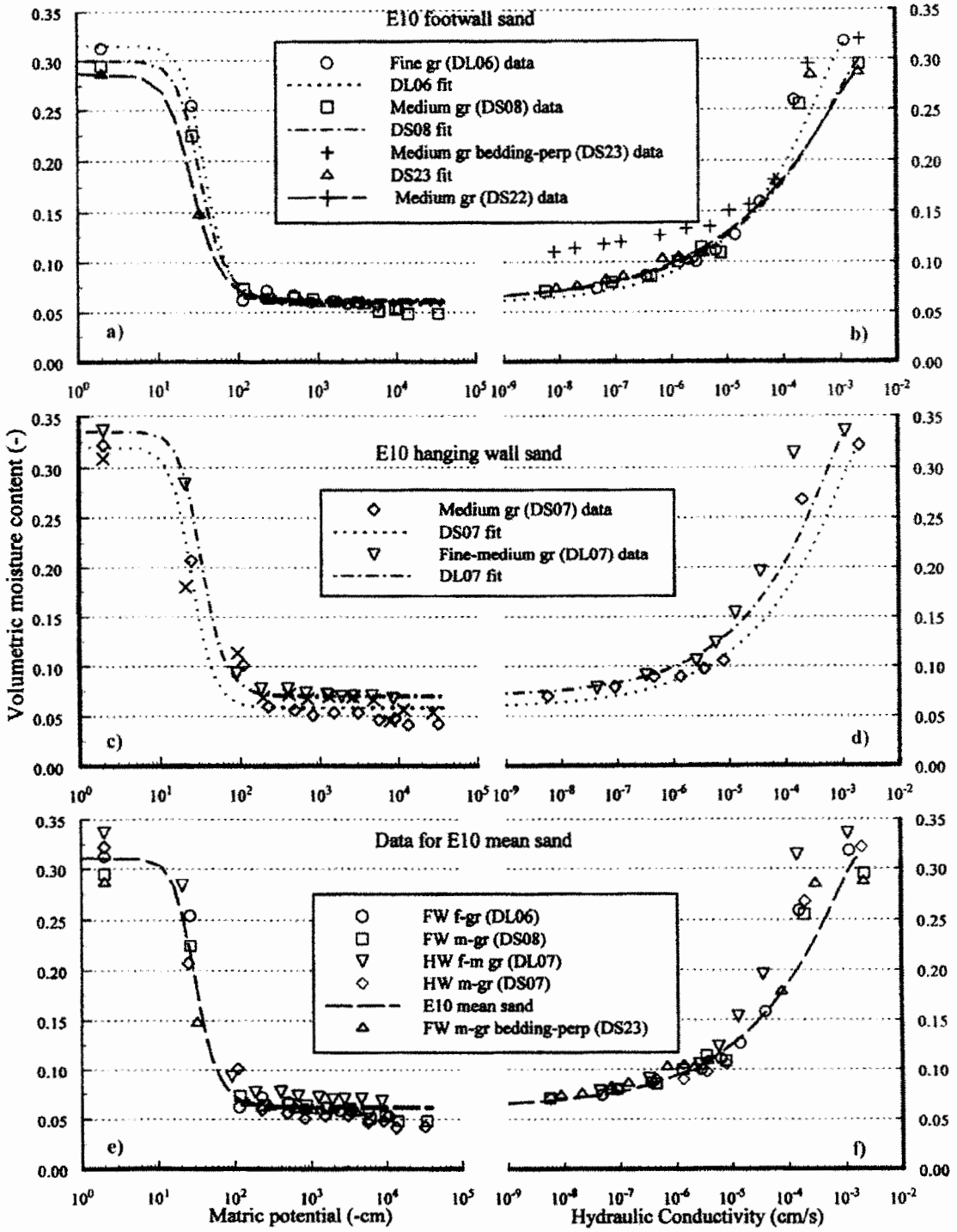

Figure A1. UFA measurements and Mualem-van Genuchten model fits for individual samples. The left-hand plots show θ-ψ results, and the right-hand plots show K-θ results. Lines depict the theoretical curves for the fitted Mualem-van Genuchten models using parameters shown in Table 3.

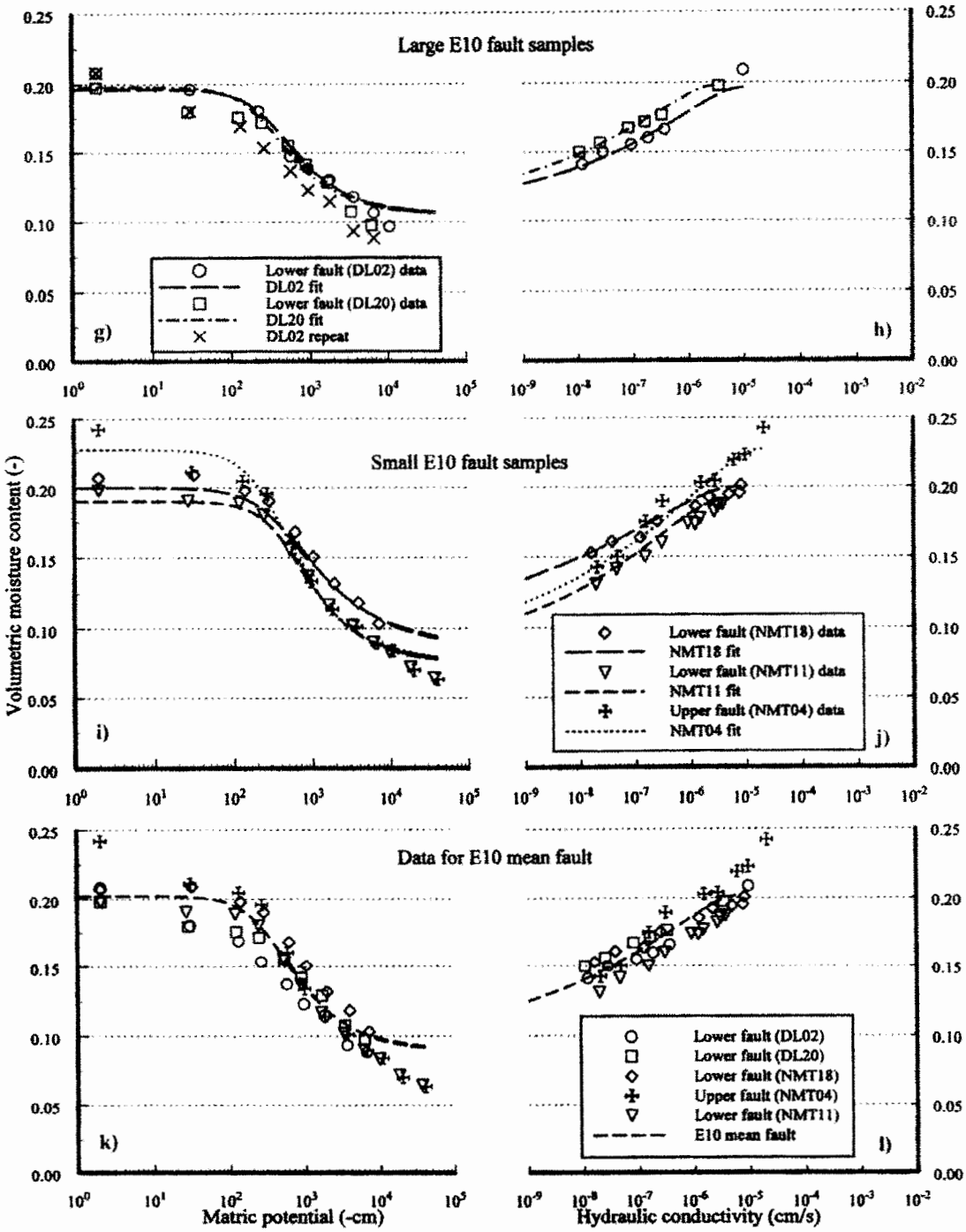

Figure A1. (continued)

paper. With at least one fault every 4 m, and assuming fault conditions are similar at depth, infiltration through the sand beds at the Canyon Trail site could be locally enhanced severalfold. Fault density is less critical when considering contaminant transport. One or more faults beneath a contaminated surface site could redistribute contaminants downward so that underlying aquifers are adversely affected. Fault "fast paths" are also more likely to experience much more rapid diagenetic alteration than the parent sand. As an example, a simple diagenesis model

relates the amount of diagenetic alteration observed in a given volume of sediments to the number of pore volumes of aqueous solution that pass through those sediments. At an ambient matric potential of −200 cm a fault will advect more than a hundred pore volumes under gravity-driven flow in the time taken to advect a single pore volume through the sand (Figure 4). Although our results indicate a propensity for faults to enhance recharge, shorten contaminant residence times, and accelerate diagenesis, more study is needed to test for hydrologic significance.

6. Conclusions

[38] Deformation band faults resulting from relatively small displacements possess strikingly different saturated and unsaturated hydraulic properties than their poorly lithified parent sands. Saturated hydraulic conductivity values for fault E10 at the Canyon Trail site are 3 orders of magnitude smaller than those for the parent sand, in good agreement with previously published values for this fault and other faults. For unsaturated conditions, fault E10 conductivity equals sand conductivity in the (crossover) matric potential range of −35 to −80 cm, a condition that is relatively high (wet) for much of the Rio Grande rift. As matric potential ψ decreases into the drier range, fault conductivity K declines much less rapidly than does sand K. For matric potentials less than −100 cm, typical for semiarid and arid zones, fault conductivity exceeds sand K by 2–6 orders of magnitude. The observed $K(\psi)$ behavior shows relatively little variability between hanging wall and footwall sand samples and between various fault samples. Under conditions of steady gravity-driven flow, faults permit downward, liquid-phase flux densities 10^2–10^6 times larger than those in their parent sands, and reduce nonreactive solute travel times by similar orders of magnitude. If our measured hydraulic properties describe faults and sands in other poorly lithified vadose zones, and we believe they do, deformation band faults can significantly enhance gravity-driven downward moisture and solute transport through vadose zones where the matric potential is much less than −100 cm. If present in sufficient density, faults encountered in semiarid and arid climates should enhance recharge, hasten contaminant migration, and accelerate diagenesis.

Appendix A: Sample Mualem-van Genuchten Model Fits

[39] Plots of K-θ and θ-ψ experimental results and final simultaneous fits to equations (1) and (2) are shown in Figure A1 for samples with complete UFA analyses.

Appendix B: Local E10 Matric Potential Estimates

[40] The larger air entry matric potentials and relatively gradual decline in the θ-ψ relations for deformation band faults (Figure 2 and Appendix A) suggest such faults may provide a very efficient means of quickly estimating the ambient matric potential at a vadose zone outcrop exposure using simple gravimetric methods and fitted θ-ψ curves. One determines in situ θ from a fault sample's volume (or bulk density) and its moisture weight, then reads off the corresponding matric potential ψ from the fault θ-ψ curve.

[41] We applied this approach at fault E10, gravimetrically measuring moisture content for four fault samples. Mean volumetric moisture content (± one standard deviation) for the fault samples was 18% (±1%). We used equation (1) inverted to solve for ψ as a function of θ, the four fault in situ moisture contents, and mean fault parameters (Table 3) to estimate the ambient matric potential near fault E10. The matric potentials of the four samples were estimated to be −187, −243, −335, and −379 cm. Using the mean moisture content of these four samples, the estimated matric potential is −283 cm. These estimates apply to a zone roughly 30 cm behind the outcrop face, and thus the ambient matric potential deeper within the outcrop is likely to be higher (closer to zero).

[42] If this approach is valid, matric potential in the adjacent sand should be similar. We can use these estimated potentials and the sand θ-ψ relationships to estimate sand moisture contents, and check these with field samples. For this range of matric potentials the sand θ-ψ curves in Figure 2 suggest that the sand should be at or near residual moisture content. Four representative samples were collected from the lower sand unit, three from the footwall, and one from the hanging wall. The mean θ was 4.7% (±1.6%), near to, as expected, but less than any of the estimated sand residual moisture content values (Table 3).

[43] **Acknowledgments.** The National Science Foundation's Hydrologic Sciences Program funded this study, grant EAR-9614385. We thank the staff of the Bosque del Apache National Wildlife Refuge and the Burlington Northern Santa Fe Railroad for access to the study site; our fellow members of New Mexico Tech's Faults and Fluid Flow group, especially Laurel Goodwin, Peter Mozley, Bill Haneberg, Matt Herrin, and Geoff Rawling for many hours of helpful discussion; James Conca, Judith Wright, and Paula Heller of UFA Ventures for access to multiple UFA systems and assistance in conducting the UFA experiments; Bob Glass of Sandia National Laboratories for use of his Flow and Transport Laboratory; John Hawley, emeritus New Mexico Bureau of Geology and Mineral Resources, for help with the geologic framework; and Bob Holt of the University of Mississippi for many fruitful discussions. We are grateful to the three anonymous reviewers for their generous efforts to improve this paper.

References

Antonellini, M., and A. Aydin, Effect of faulting on fluid flow in porous sandstones: Petrophysical properties, *AAPG Bull.*, *78*, 355–377, 1994.

Antonellini, M., A. Aydin, and D. Pollard, Microstructure of deformation bands in porous sandstones at Arches National Park, Utah, *J. Struct. Geol.*, *16*, 941–959, 1994.

Aydin, A., Small faults formed as deformation bands in sandstone, *Pure Appl. Geophys.*, *116*, 913–930, 1978.

Brainard, J. R., Vadose zone flow processes in heterogeneous alluvial fan deposits: Experimental design, data evaluation, and error analysis, M.S. thesis, Dep. of Geol., Univ. of N. M., Albuquerque, 1997.

Brainard, J. R., R. J. Glass, D. L. Alumbaugh, L. Paprocki, D. J. Labrecque, X. Yang, T.-C. J. Yeh, K. E. Baker, and C. A. Rautman, The Sandia-Tech Vadose Zone Facility experimental design and data report of a constant flux infiltration experiment, *Rep. SAND02-2168*, Sandia Natl. Lab., Albuquerque, N. M., 2002.

Brooks, R. H., and A. T. Corey, Hydraulic properties of porous media, *Hydrol. Pap 3*, Colo. State Univ., Fort Collins, Colo., 1964.

Caine, J. S., J. P. Evans, and C. B. Forster, Fault zone architecture and permeability structure, *Geology*, *24*, 1025–1028, 1996.

Carter, K. E., and C. L. Winter, Fractal nature and scaling of normal faults in the Espanola Basin, Rio Grande Rift, New Mexico: Implications for fault growth and brittle strain, *J. Struct. Geol.*, *17*, 863–873, 1995.

Cashman, S., and K. Cashman, Cataclasis and deformation-band formation in unconsolidated marine terrace sand, Humboldt County, California, *Geology*, *28*, 111–114, 2000.

Chamberlin, R. M., and G. R. Osborn, Character and evolution of extensional domains in the Socorro area of the Rio Grande Rift, central New Mexico, *Geol. Soc. Am. Abstr. Programs*, *16*(6), 467, 1984.

Chapin, C. E., and S. M. Cather, Tectonic setting of the axial basins of the northern and central Rio Grande Rift, in *Basins of the Rio Grande Rift: Structure, Stratigraphy, and Tectonic Setting*, edited by G. R. Keller and S. M. Cather, *Geol. Soc. Am. Spec. Pap.*, *291*, 5–26, 1994.

Conca, J. L., and J. V. Wright, Diffusion coefficients in gravel under unsaturated conditions, *Water Resour. Res.*, *26*, 1055–1066, 1990.

Conca, J. L., and J. V. Wright, Flow and diffusion in unsaturated gravel, soil and whole rock, *Appl. Hydrogeol.*, *1*, 5–24, 1992.

Conca, J. L., and J. V. Wright, The UFA method for rapid, direct measurements of unsaturated transport properties in soil, sediment, and rock, *Aust. J. Soil Res.*, *36*, 291–315, 1998.

Conca, J., D. Levitt, P. Heller, T. Mockler, and M. Sully, Direct UFA measurements of unsaturated hydraulic conductivity, comparisons to van Genuchten/Mualem estimations, and applications to recharge mapping in arid regions, in *Proceedings of the International Workshop on Characterization and Measurement of the Hydraulic Properties of Unsaturated Porous Media*, edited by M. T. van Genuchten, F. J. Leij, and L. Wu, pp. 1173–1197, Univ. of Calif., Riverside, 1999.

Connell, S. D., D. J. Koning, and S. M. Cather, Revisions to the stratigraphic nomenclature of the Santa Fe Group, northwestern Albuquerque Basin, New Mexico, *Field Conf. Guideb. N. M. Geol. Soc.*, *50*, 337–353, 1999.

Edwards, H. E., A. D. Becker, and J. A. Howell, Compartmentalization of an eolian sandstone by structural heterogeneities: Permo-Triassic Hopeman sandstone, Moray Firth, Scotland, in *Characterization of Fluvial and Aeolian Reservoirs*, edited by C. P. North and D. J. Prosser, pp. 339–365, Geol. Soc., London, 1993.

Flint, L. E., D. B. Hudson, and A. L. Flint, Unsaturated hydraulic parameters determined from direct and indirect methods, in *Proceedings of the International Workshop on Characterization and Measurement of the Hydraulic Properties of Unsaturated Porous Media*, edited by M. T. van Genuchten, F. J. Leij, and L. Wu, pp. 293–302, Univ. of Calif., Riverside, 1999.

Forbes, P. L., Simple and accurate methods for converting centrifuge data into drainage and imbibition capillary pressure curves, *Log Anal.*, *35*, 31–53, 1994.

Fowles, J., and S. Burley, Textural and permeability characteristics of faulted, high porosity sandstones, *Mar. Petrol. Geol.*, *11*, 608–623, 1994.

Grauch, V. J., High-resolution aeromagnetic data, a new tool for mapping intrabasinal faults: Example from the Albuquerque basin, New Mexico, *Geology*, *29*, 367–370, 2001.

Hassler, G. L., and E. Brunner, Measurement of capillary pressures in small core samples, *Trans. AIME*, *160*, 114–123, 1945.

Hawley, J. W. (Comp.), *Guidebook to Rio Grande Rift in New Mexico and Colorado*, N. M. Bur. of Mines and Miner. Resour., Socorro, N. M., 1978.

Hawley, J. W., and J. M. Kernodle, Overview of the hydrogeology and geohydrology of the northern Rio Grande basin—Colorado, New Mexico, and Texas, in *Proceedings of the 44th Annual New Mexico Water Conference*, edited by C. T. Ortega-Klett, pp. 79–102, *Rep. 312*, N. M. Water Resour. Res. Inst., Las Cruces, N. M., 2000. (Available at http://wrri.nmsu.edu/publish/watcon/proc/proc44/contents.html)

Hawley, J. W., C. S. Haase, and R. P. Lozinsky, An underground view of the Albuquerque Basin, New Mexico, in *Proceedings of the 39th Annual New Mexico Water Conference*, edited by C. T. Ortega-Klett, *Rep. 290*, pp. 37–55, N. M. Water Resour. Res. Inst., Las Cruces, N. M., 1995.

Hawley, J. W., J. F. Kennedy, and B. J. Creel, The Mesilla Basin aquifer system of New Mexico, West Texas and Chihuahua—An overview of its hydrogeologic framework and related aspects of groundwater flow and chemistry, in *Aquifers of West Texas: Texas Water Development Board Special Conference Proceedings Volume*, edited by E. S. Angle and R. E. Mace, pp. 76–99, 2001. (Available at http://www.twdb.state.tx.us/publications/reports/GroundWaterReports/GWReports/Individual%20-Report%20htm%20files/Report%20356.htm)

Herrin, J. M., Characteristics of deformation bands in poorly lithified sand: Rio Grande Rift, New Mexico, M.S. thesis, Dep. of Geol., N. M. Inst. of Mining and Technol., Socorro, N. M., 2001.

Heynekamp, M. R., L. B. Goodwin, P. S. Mozley, and W. C. Haneberg, Controls on fault-zone architecture in poorly lithified sediments, Rio Grande Rift, New Mexico: Implications for fault-zone permeability and fluid flow, in *Faults and Subsurface Fluid Flow in the Shallow Crust, Geophys. Monogr. Ser.*, vol. 13, edited by W. C. Haneberg et al., pp. 27–49, AGU, Washington, D. C., 1999.

Hong, S., Anisotropic hydraulic conductivity of faulted poorly consolidated eolian sands: Bosque, New Mexico, M.S. thesis, Dep. of Geol., N. M. Inst. of Mining and Technol., Socorro, N. M., 1999.

Khaleel, R., J. F. Relyea, and J. L. Conca, Estimation of van Genuchten-Mualem relationships to estimate unsaturated hydraulic conductivity at low water contents, *Water Resour. Res.*, *31*, 2659–2668, 1995.

Mattson, E. D., Field simulation of waste impoundment seepage in the vadose zone: Experiment design in two dimensional modeling, M.S. thesis, Dep. of Hydrol., N. M. Inst. of Mining and Technol., Socorro, N. M., 1989.

McCord, J. T., D. B. Stephens, and J. L. Wilson, Hysteresis and state-dependent anisotropy in modeling unsaturated hillslope hydrologic processes, *Water Resour. Res.*, *27*, 1501–1518, 1991.

Mualem, Y., A new model for predicting the hydraulic conductivity of unsaturated porous media, *Water Resour. Res.*, *12*, 513–522, 1976.

Nimmo, J. R., J. Rubin, and D. P. Hammermeister, Unsaturated flow in a centrifugal field: Measurement of hydraulic conductivity and testing of Darcy's law, *Water Resour. Res.*, *23*, 124–134, 1987.

Ogilvie, S. R., J. M. Orribo, and P. W. Glover, The influence of deformation bands upon fluid flow using profile permeametry and positron emission tomography, *Geophys. Res. Lett.*, *28*, 61–64, 2001.

Pittman, E. D., Effect of fault-related granulation on porosity and permeability of quartz sandstones, Simpson Group (Ordovician), Oklahoma, *AAPG Bull.*, *65*, 2381–2387, 1981.

Rawling, G. C., L. B. Goodwin, and J. L. Wilson, Internal architecture, permeability structure, and hydrologic significance of contrasting fault-zone types, *Geology*, *29*, 43–46, 2001.

Ross, B., A conceptual model of deep unsaturated zones with negligible recharge, *Water Resour. Res.*, *28*, 1627–1629, 1984.

Scanlon, B. R., S. W. Tyler, and P. J. Wierenga, Hydrologic issues in arid, unsaturated systems and implications for contaminant transport, *Rev. Geophys.*, *35*, 461–490, 1997.

Sigda, J. M., Preferential flow and transport through deformation band faults in the semi-arid vadose zone of the Rio Grande Rift, New Mexico, USA, Ph.D. thesis, Dep. of Hydrol., N. M. Inst. of Mining and Technol., Socorro, N. M., 2003.

Sigda, J. M., L. B. Goodwin, P. S. Mozley, and J. L. Wilson, Permeability alteration in small-displacement faults in poorly lithified sediments; Rio Grande Rift, central New Mexico, in *Faults and Subsurface Fluid Flow in the Shallow Crust, Geophys. Monogr. Ser.*, vol. 113, edited by W. C. Haneberg et al., pp. 51–68, AGU, Washington, D. C., 1999.

Smith, L., C. Forster, and J. Evans, Interaction of fault zones, fluid flow, and heat transfer at the basin scale, in *Hydrogeology of Low Permeability Environments*, edited by S. P. Neuman and I. Neretnieks, pp. 41–67, Verlag Heinz Heise, Hannover, Germany, 1989.

Stephens, D. B., and R. Knowlton Jr., Soil water movement and recharge through sand at a semiarid site in New Mexico, *Water Resour. Res.*, *22*, 881–889, 1986.

Taylor, W. L., and D. D. Pollard, Estimation of in situ permeability of deformation bands in porous sandstone, Valley of Fire, Nevada, *Water Resour. Res.*, *36*, 2595–2606, 2000.

van Genuchten, M. T., A closed-form equation for predicting the hydraulic conductivity of unsaturated soils, *Soil Sci. Soc. Am. J.*, *44*, 892–898, 1980.

van Genuchten, M. T., F. J. Leij, and S. R. Yates, The RETC code for quantifying the hydraulic functions of unsaturated soils, *Rep. EPA/600/2-91/065*, U.S. Environ. Prot. Agency, Cent. Environ. Res. Inf., Cincinnati, Ohio, 1991.

Wright, J. V., J. L. Conca, and X. Chen, Hydrostratigraphy and recharge distributions from direct measurements of hydraulic conductivity using the UFA® method, *Tech. Rep. PNL-9424*, Pac. Northwest Lab., Richland, Washington, 1994.

J. M. Sigda and J. L. Wilson, Department of Earth and Environmental Science, New Mexico Institute of Mining and Technology, Socorro, NM 87801, USA. (sigda@nmt.edu)